$c(2\times2)$Cl/Cu(001) adsorbate geometry and substrate-surface relaxation using low-temperature angle-resolved photoemission extended fine structure

Li-Qiong Wang, A. E. Schach von Wittenau, Z. G. Ji,* L. S. Wang, Z. Q. Huang, and D. A. Shirley
Department of Chemistry, University of California, Berkeley, California 94720
and Chemical Sciences Division, Lawrence Berkeley Laboratory, Berkeley, California 94720
(Received 10 December 1990)

A detailed structural study of the $c(2\times2)$Cl/Cu(001) adsorbate system was made, using the angle-resolved photoemission extended-fine-structure (ARPEFS) technique at low temperature, which yields both more accurate surface structural information and near-surface structural information for deeper substrate layers. Electrons were detected along two emission directions, [001] and [011], and at two temperatures, 110 and 300 K. The Cl atoms were found to adsorb in the fourfold hollow site, 1.604(5) Å above the first copper layer, with a Cl—Cu bond length of 2.416(3) Å (in which the errors in parentheses are statistical standard deviations only). These values are in excellent agreement with a previous low-energy electron-diffraction study by Jona *et al.* The $c(2\times2)$Cl-covered first copper layer showed no relaxation with respect to the bulk position. However, a small corrugation of the second copper layer was found: The second-layer copper atoms below the Cl atoms move 0.042(12) Å away from the surface, while those in open positions remain in their bulk positions. The distances from the Cl atoms to the third and fourth copper layers were found to be 5.222(25) and 7.023(22) Å, respectively, yielding a bulk-like interlayer spacing. Thus the depth sensitivity of the low-temperature ARPEFS facilitated definitive referencing of near-surface atomic positions to the underlying lattice.

I. INTRODUCTION

There is chemical and physical interest in detailed surface structures, and in adsorbate-induced substrate relaxation. Techniques such as low-energy electron diffraction (LEED),[1] surface extended x-ray-absorption fine structure (SEXAFS),[2] medium-energy ion scattering,[3] the x-ray standing-wave method,[4] and angle-resolved photoemission extended fine structure (ARPEFS)[5] have been used to study surface structures. However, a complete knowledge of adsorbate-induced substrate surface relaxation requires a reliable and accurate determination of both the surface and the near-surface structure, including the deeper substrate layers. ARPEFS may prove to be uniquely suitable in this regard among surface-structural techniques, because of its depth sensitivity to $\sim4-5$ atomic layers. The main contribution of this paper is to demonstrate this capability of ARPEFS by example: we determine the adsorbate geometry and the substrate surface relaxation of $c(2\times2)$Cl/Cu(001) using low-temperature ARPEFS. The key point is that cooling the lattice effectively extends the range of ARPEFS to the fourth copper layer, thereby firmly referencing atomic positions in the surface and near surface layers to the bulk crystal lattice.

ARPEFS is a novel technique for studying surface structures using photoelectron diffraction.[6] Using the phenomenon of photoelectron diffraction as a probe of surface structure was originally proposed by Liebsch[7,8] and was observed experimentally by three groups independently.[9–11] Initially, our group employed normal photoelectron diffraction,[12,13] in which oscillations over a limited low-energy range were fitted with a LEED-like theory to derive structures. Later, ARPEFS, which is formally analogous to extended x-ray-absorption fine structure (EXAFS) was developed. In ARPEFS, one measures the angle-resolved photoemission intensity from a core level of the adsorbate as a function of the photoelectron kinetic energy over a wide energy range (typically $=50-500$ eV). Photoelectrons from the adsorbate can be elastically scattered by neighboring atoms: the measured photoemission intensity contains surface structural information due to the final-state interference. Unlike LEED, ARPEFS allows qualitative data analyses by Fourier transformation, giving rather direct access to the structural information. This is similar to SEXAFS, but ARPEFS yields path-length differences while SEXAFS gives interatomic distances between the adsorbate (source) and substrate (scattering) atoms. A quantitative structural analysis by ARPEFS requires multiple-scattering spherical-wave (MSSW) theory,[14] while single scattering is usually applied in SEXAFS. With a MSSW level analysis, effects as subtle as small corrugation and relaxation near the substrate surface can be characterized. More recently, an ARPEFS study of $c(2\times2)$S/Cr(001) (Ref. 15) has provided new experimental insight into the depth to which ARPEFS can probe into the substrate surface. For this stiff lattice (high Debye temperature), path-length differences greater than 10 Å were discernable and were successfully modeled by the MSSW calculations. By performing ARPEFS measurements at low temperatures similar advantages would be expected with softer lattices.

In this paper we report the first low-temperature

ARPEFS study on an atomic adsorbate system. We chose the $c(2\times2)$Cl/Cu(001) system for several reasons. First, we believed that a detailed study of the surface and near-surface structure of $c(2\times2)$Cl/Cu(001) at such a high level of accuracy that the substrate surface relaxation including small corrugation can be revealed might resolve some discrepancies in the literature. In a LEED study, Jona *et al.*[1] determined that the Cl atoms adsorb in the fourfold symmetric hollow sites with a Cl-Cu interlayer spacing of 1.60(3) Å and a slightly expanded Cu-Cu first interlayer spacing of 1.85(3) Å. However, a Cl-Cu interlayer spacing of 1.53(2) Å was derived from a SEXAFS bond length of 2.37(2) Å in SEXAFS studies,[2,16] and Patel *et al.*[17] reported substrate surface relaxation for $c(2\times2)$Cl/Cu(001) by using a combination of x-ray standing wave and SEXAFS techniques, finding a 0.07(4) Å outward relaxation of the first copper layer. Indeed, both the LEED and SEXAFS studies have shown the expansion of the Cu-Cu first interlayer spacing. An interesting question is the following: how does the substrate relax in this expansion? Is it an outward relaxation of the first copper layer, or a downward relaxation of the second copper layer, or do both the first and second copper layer move? Another motivation for this work was to study the surface-atom vibrational anisotropy using temperature-dependent ARPEFS. That part of the work will be reported separately.

This paper is organized as follows. Section II gives the experimental details. Section III describes the procedures of data collection and reduction, and presents results of two types of analysis used to extract structural information: Fourier and multiple-scattering analysis. Section IV discusses and compares the results. A summary and conclusions are given in Sec. V.

II. EXPERIMENT

The experiments were performed at the Stanford Synchrotron Radiation Laboratory on Beamline III-3 using a Ge(111) double-crystal monochromator. The Cl 1*s* photoemission spectra were taken in the kinetic energy range from 50 to 550 eV with photon energies from 2870 to 3370 eV. The resolution of the double-crystal monochromator was approximately 2 eV through this photon energy range. The double Bragg reflection geometry significantly enhanced the already high degree of linear polarization of the incident synchrotron radiation.[18] A polarization of $\geq 98\%$ was achieved.

The photoemission spectra were collected with a hemispherical electrostatic analyzer described previously.[19] The analyzer is mounted on a carriage which allows rotating under UHV conditions of 360° about a vertical axis and 100° about a horizontal axis. Under the operating conditions of 160-eV pass energy, the energy resolution of the analyzer is ~ 1 eV full width at half maximum and the angular resolution of the input lens is ±3°. The UHV experimental chamber also contains a four-grid LEED system for doing LEED and Auger electron spectroscopy (AES), an ion gun, and an effusive beam doser for sample preparation.

A copper single crystal was cut, oriented to within ±1° of the [001] direction as determined by Laue backscattering, then mechanically polished and chemically etched. The final finished crystal was mounted on a high precision manipulator with a liquid-nitrogen cooling system, allowing enough motion to adjust the orientation of the sample. In the low-temperature measurements, the sample was cooled to 110±5 K as measured by a chromel-alumel thermocouple attached to the sample. The clean Cu surface was prepared by repeated Ar^+-ion sputtering and annealing to about 850 K until AES showed no carbon, nitrogen, oxygen, or sulfur contamination and a sharp $p(1\times1)$ (LEED) pattern was observed. The Cu(001) surface was exposed to Cl_2 through an effusive beam doser. A sharp $c(2\times2)$ Cl overlayer LEED pattern was produced by dosing Cl_2 at room temperature for about 2 min with the main chamber pressure below 5×10^{-9} Torr. This was followed by a 400-K annealing for 2 min to completely dissociate Cl_2 into atomic Cl.

The pressure in the experimental chamber was between 2×10^{-10} and 6×10^{-11} Torr during all the measurements. The sample was flashed to about 400 K every 6–9 h during data collection, and more often for the low-temperature measurements. The ARPEFS measurements were performed at room temperature and 110±5 K, and along the two emission directions [001] and [011] at each temperature. The experimental directions were determined by a He-Ne laser autocollimation referenced to the experimental viewports with an accuracy of ±2°. The experimental geometries are shown in Fig. 1. For the [001] geometry, photoelectrons were collected along the surface normal with the photon polarization vector 35° from the surface normal toward the [011] direction. The other geometry, with the photon polarization vector 48° off the surface normal almost lying the [011] direction and with

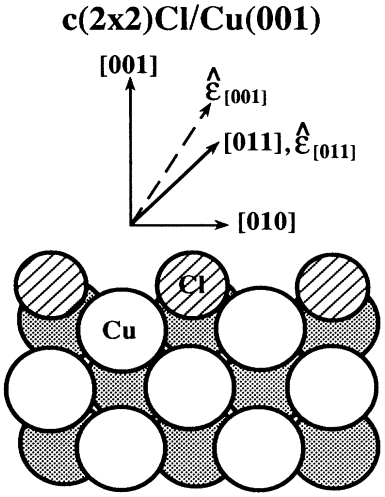

FIG. 1. A side view of the $c(2\times2)$Cl/Cu(001) structure with the experimental geometries. The emission directions are labeled as [001] and [011], while the photon polarization vectors associated with each geometry are labeled as $\hat{\varepsilon}_{[001]}$ and $\hat{\varepsilon}_{[011]}$, respectively. The larger circles represent the copper atoms. The open circles are in the same plane as the Cl atoms, while the shaded circles lie in planes above and below the paper.

the emission direction colinear with the photon polarization vector, simply called the [011] geometry for convenience in the discussion below. These two geometries were chosen to highlight nearby backscattering atoms, utilizing the directional sensitivity of ARPEFS. Backscattering in the [001] emission direction is most sensitive to the substrate copper atoms directly below the Cl atoms. Emission along the [001] direction can thus determine interlayer spacings effectively. The [011] emission direction was selected to emphasize the substrate copper atoms along the [011] direction, including the nearest neighbors.

III. DATA ANALYSIS AND RESULTS

In this section we describe the procedures for reducing a series of photoelectron spectra into $\chi(k)$ curves, which contain the surface structural information. This information was extracted from the $\chi(k)$ curves in two ways: by Fourier analysis and by multiple-scattering spherical-wave (MSSW) analysis. Fourier analysis gave the adsorption site and approximate geometrical parameters. More precise values were obtained by comparing the experimental data to the MSSW calculations using an R factor (reliability factor) as a quantitative measure of the fit. An automatic routine was used to search the structural parameters at the minimum R factor. Detailed procedures are described below.

A. Data reduction

Four sets of ARPEFS data, at two geometries and two temperatures, were taken on separately prepared samples. A series of 80–100 photoemission spectra was taken for a given data set, in equal electron wave-number increments $\Delta k=0.08-0.10$ Å^{-1}. Each photoemission spectrum was centered on the Cl 1s photoelectron peak, with an energy window of 25–30 eV. In the energy region where Auger peaks appeared (181 eV), an increment of 0.08 Å^{-1} and an energy window of 30 eV were used.

In recent ARPEFS studies,[15,20] a Voigt function (Gaussian convoluted with a Lorentzian) was used to model the photoelectron peak, to account for lifetime broadening (Lorentzian) of the core hole and instrumental broadening (Gaussian) due to the monochromator and analyzer resolution. The Voigt function was found to fit the core-level photoelectron peak more accurately than a pure Gaussian function. In this work, each individual photoemission spectrum was fitted with three functions: a Voigt function to model the core-level photoelectron peak, a Gaussian convoluted with a step function (G step) to describe the inelastically scattered electrons associated with the photoelectron peak, and an experimentally measured background to account for other inelastic scattering processes. The quantity of interest was the area of the Voigt peak. It was necessary to normalize each photoemission spectrum to compensate for the irregularities in the photon flux, as well as for the analyzer transmission function. The experimental background consisted of three photoemission scans covering the kinetic energy range of 40–550 eV. Each scan was taken at a different photon energy so that the Cl 1s photoelectron peak lay about 10 eV below the lowest kinetic energy in each spectrum. A "master" background curve was taken for each geometry and temperature. It was used both for the least-squares fitting and for the normalization of each photoemission spectrum.

Since the Lorentzian width due to lifetime broadening is independent of the experimental conditions, it was fixed in the least-squares fittings for all the photoemission spectra. The width of the G step was kept at the same value as the width of the Gaussian part of the Voigt function. Lorentzian widths in the range of 1.0–1.5 eV, which is somewhat larger than the natural K-shell linewidth of 0.65 eV for Cl calculated by Krause and Oliver,[21] gave equally good fits. A final value of 1.5 eV was used. Each individual photoemission spectrum was normalized by a scale factor to the background function obtained in the least-square fitting. The total photoemission intensity $I(E)$ was generated by plotting the area of each Voigt function as a function of the photoelectron kinetic energy taken as the mean energy of each Voigt function. The final $I(E)$ curve was divided by the kinetic energy to compensate for the analyzer transmission function.

In analogy to EXAFS, the total photoemission intensity $I(E)$ consists of a slowly varying atomiclike function and an oscillating contribution caused by the interference effects. $I(E)$ can then be described as

$$I(E)=[\chi(E)+1]I_0(E)\ , \tag{1}$$

where $I_0(E)$ is a slowly varying atomiclike function and $\chi(E)$ is the oscillatory interference function which can be determined by removing the slowly varying function $I_0(E)$ from the total photoemission intensity $I(E)$:

$$\chi(E)=\frac{I(E)-I_0(E)}{I_0(E)}\ . \tag{2}$$

This is finally the function of interest in ARPEFS, analogous to EXAFS.

Theoretically, $I_0(E)$ is essentially the Cl 1s atomic cross section, which can in principle be calculated from the atomic wave functions. In reality, since the exact form of $I_0(E)$ is not completely known and $I_0(E)$ contains only the very-low-frequency part of $I(E)$, a low-order polynomial or a smooth cubic spline has been applied to simulate $I_0(E)$, in analogy with EXAFS.[22] Experimentally, however, the low-frequency part of $I(E)$ contains not only the slowly varying atomiclike cross section but also some ARPEFS structures at low path-length differences, as well as any contributions introduced by the processes of data collection and experimental conditions. For example, movements of the photon beam and changes in the slope of the experimentally measured background during data collection would give rise to low-frequency components in the $\chi(E)$ curves. The choices of appropriate $I_0(E)$ were made by requiring the minimal intensity of the Fourier amplitude at zero path length in some of the previous studies.[15,23] However, this choice of $I_0(E)$ is arbitrary, and the $\chi(E)$ curves generated by using different low-order polynomials can vary. The structural information at the scattering path-length differences less than about 1.5–2.0 Å is therefore not reli-

able, being either distorted or completely removed. Since there can be no real structural information contained in the path-length differences less than 2 Å for the [001] data and 1.5 Å for the [011] data, low-order polynomials were first used to construct $\chi(E)$ curves in the current study, then Fourier filtering was applied to filter out the frequencies below those values. The resulting $\chi(E)$ curves are independent of the choices of the low-order polynomials. In comparing the experimental results with theory, the same procedures were used to filter the theoretical curves.

The experimental $\chi(E)$ curves are shown in Figs. 2 and 3 for the [001] and [011] data, respectively, at the two different temperatures. It is clear that the oscillation amplitudes of $\chi(E)$ at the lower temperature are greatly enhanced as compared with those at room temperature. The oscillation patterns are matched very well at the two temperatures.

Once reliable $\chi(E)$ curves were obtained, they were converted to $\chi(k)$ for the purposes of Fourier transformation and comparison with theory, using the de Broglie relation:

$$k=\hbar^{-1}\sqrt{2m_e(E+V_0)}\ , \tag{3}$$

where m_e is the electron rest mass and V_0 is the inner potential of the solid. The exact value of V_0 is unknown, but for copper V_0 is around 10 eV. We treated V_0 as an adjustable parameter in the fits, and determined its value as 10±2 eV.

B. Fourier analysis

Fourier analysis of the $\chi(k)$ curve in ARPEFS yields the path-length differences

$$\Delta R_j=r_j(1-\cos\theta_j)\ , \tag{4}$$

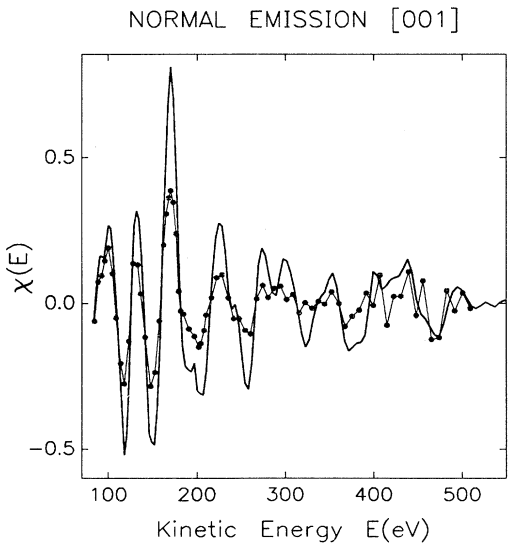

FIG. 2. Experimental $\chi(k)$ curves for the [001] geometry. The curve with solid dots is $\chi(k)$ at 300 K, and the heavier curve is $\chi(k)$ at 110 K.

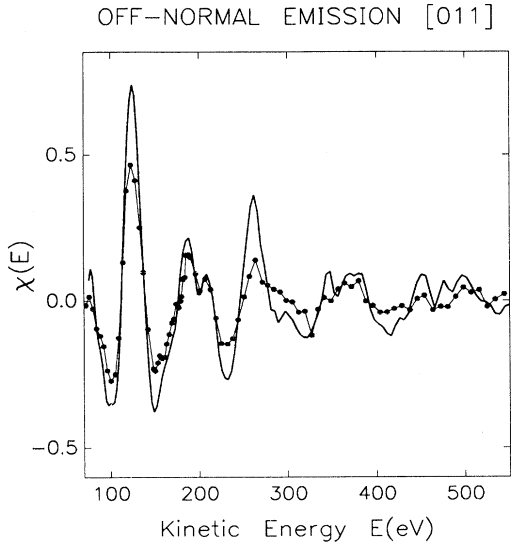

FIG. 3. Experimental $\chi(k)$ curves for the [011] geometry at two temperatures, as in Fig. 2.

which follows from single-scattering ARPEFS theory which gives

$$\chi(k)=2\sum_j A_j(k)e^{-\sigma_j^2(1-\cos\theta_j)k^2} \times\cos[kr_j(1-\cos\theta_j)+\phi_j]\ , \tag{5}$$

where $A_j(k)$ contains the elastic scattering amplitude modified by the inelastic losses and aperture integration, r_j is the distance between the photoemitter and jth scattering atom, θ_j is the scattering angle at the jth atom, and ϕ_j is the scattering phase shift. The temperature effect is introduced as a Debye-Waller factor, where σ_j is the mean-square relative displacement between the photoemitter and the jth scattering atom, projected on the photoelectron momentum change direction. The Fourier peaks appear at the path-length differences ΔR_j. Structural information can therefore be obtained directly from the Fourier spectrum of each emission geometry.

The Fourier transformation procedure was described previously.[5] Fourier spectra for the [001] and [011] data at the two temperatures are given in Figs. 4 and 5, respectively. In each case, the spectral features agree very well for the two temperatures, while the amplitudes at the lower temperature are enhanced. Strong Fourier peaks are present even at path-length differences greater than 10 Å for the lower-temperature spectra. This is more prominent for the [001] data where real spectral features up to 20 Å path-length difference are evident. Thus, scattering from deeper substrate layers makes significant contributions to the ARPEFS signal at low temperature, providing an opportunity to extract both surface and near-surface structural information more accurately.

It is known from previous LEED (Ref. 1) and SEXAFS (Ref. 2) studies that the Cl atom adsorbs at the fourfold hollow site of the Cu(001) surface. We can in fact obtain this adsorption geometry simply by Fourier analysis of

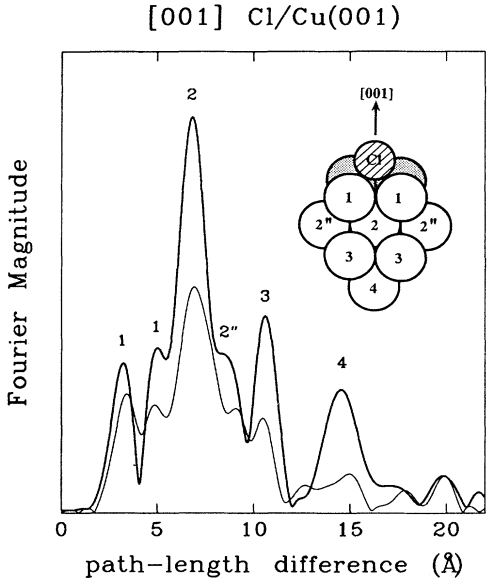

FIG. 4. Fourier spectra for the [001] geometry at two temperatures, 110 and 300 K, respectively. Each numbered peak is associated with a scattering path-length difference for a numbered atom in the inset.

the ARPEFS data. Forward ($\theta_j=0°$) and backward ($\theta_j=180°$) scatterings give the strongest signals in the k range of our data. However, for adsorbate source atoms, forward scattering alone does not occur in our geometries, which were chosen to highlight the backscatterers. Thus, backscattering provides the strongest ARPEFS signals, producing the dominant peak evident

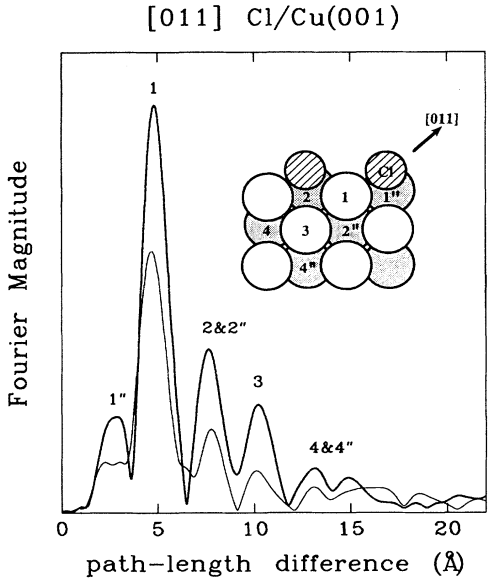

FIG. 5. Fourier spectra for the [011] geometry at two temperatures, 110 and 300 K, respectively. Each numbered peak is associated with a scattering path-length difference for a numbered atom in the inset.

in each Fourier spectrum. From Eq. (4), the strongest peak due to backward scattering should appear at a path-length difference $\Delta R_j \approx 2r_j$ if a near-neighbor substrate atom lies at a distance r_j directly behind the adsorbate atom. In Fig. 4 the strong peak at $\Delta R_j \sim 6.9$ Å in the [001] direction is thus assigned to the Cu atom directly below the Cl atom. An atop adsorption site could be considered as an alternative candidate structure. But a Cl atom in an atop site would then have a bond length of ~ 3.45 Å, too long for the Cl—Cu bond, and the peaks at ~ 3.3 and ~ 5.0 Å would be unexplained. In addition, an atop site would not give a 4.8-Å peak in the [011] emission data, thus an atop site is excluded. The peak at ~ 4.8 Å offers a reasonable estimate of the bond length of ~ 2.4 Å for either a bridge site or a fourfold hollow site. However, a bridge site, having no strong backscatterer, would not give a strong peak at ~ 6.9 Å in the [001] emission direction. Therefore, the fourfold hollow site is the favored high-symmetry adsorption site for the $c(2\times 2)$Cl/Cu(001) system, in agreement with previous LEED (Ref. 1) and SEXAFS (Refs. 2 and 16) results. Similar arguments rule out alternative lower-symmetry sites.

Once the adsorption site is determined, the main features in the Fourier analysis can provide qualitative structural information about the $c(2\times 2)$Cl/Cu(001) system. Since multiple scattering is initially forward focusing, which does not introduce an additional path-length difference, the relatively strong and distinctive Fourier peaks can usually be assigned to specific scattering path-length differences, with the proviso that a given peak can arise from two or more sites. Let us discuss the [011] Fourier spectra shown in Fig. 5 first. The peak at ~ 2.8 Å corresponds to scattering through an angle of $\sim 116°$ from two nearest-neighbor atoms symmetrically located at either side of the plane containing the [001] and [011] directions, and the strongest peak at ~ 4.8 Å, to backscattering from the one of the four nearest-neighbor atoms that lies directly behind Cl along the [011] direction. This gives a Cl—Cu bond length of ~ 2.4 Å, yielding a vertical distance of Cl to the first copper layer of ~ 1.6 Å. Scattering from the nearest-neighbor atom at $\theta_j \approx 84°$ is almost negligible, because $\cos 84° = 0.10$ in Eq. (5). If we consider a (011) plane including an atom labeled 1 in Fig. 5 as the first (011) plane perpendicular to the emission direction, the two peaks at ~ 7.6 and ~ 10.2 Å can be attributed mainly to scattering from the atoms in the second and third Cu(011) planes, respectively. The peaks at ~ 13.0 and ~ 15.0 Å should correspond largely to scattering from the fourth and fifth Cu(011) layers. These two peaks have more complicated origins, because at these high path-length differences scattering processes are very complicated: multiple scattering becomes important, and many scatterers are involved.

A similar analysis can be applied to the [001] Fourier spectra, shown in Fig. 4. As noted earlier, the strongest peak, at ~ 6.9 Å, is due to backscattering from the second-layer copper atom directly below Cl, giving a ~ 3.45-Å separation between Cl and this atom. Together with the first-layer spacing of 1.6 Å, this already suggests a larger interlayer spacing than the bulk spacing (1.807

Å). The Fourier features at path-length differences from 6.9 to 10.0 Å arise mostly from scattering by atoms in the second copper layer. The relatively strong Fourier peaks at high-path-length differences ~10.7 and ~15.0 Å in the lower temperature data contain structural information from deeper substrate layers than do the room-temperature data. The peak at ~10.7 Å has a large contribution from the four atoms in the third copper layer, while the broad peak at ~15.0 Å includes mainly scattering from atoms in the fourth copper layer. The peaks at ~3.3 and ~5.0 Å arise predominantly from scattering through 131° by the four nearest-neighbor atoms, which have a geometric path-length difference of ~4.0 Å, where no peak is observed in the [001] Fourier spectra. The generalized Ramsauer-Townsend effect[5,23] causes peak splitting.

We have thus obtained approximate geometric structural parameters by assigning the main Fourier peaks. However, several factors limit this method to a qualitative analysis. First, one usually cannot simply attribute a peak to a single type of scattering process, because multiple scattering is involved and many scattering paths can give approximately the same path-length difference, especially at higher path-length differences. Furthermore, a path-length difference directly derived from the Fourier analysis contains not only the geometric difference but also the scattering phase shift ϕ_j shown in Eq. (5). Unfortunately, the back transformation of Fourier spectra cannot completely separate the geometric path-length difference from the scattering phase shift because of single and multiple scattering involved in the effective phase shift. Therefore, MSSW calculations are required to obtain quantitative structural information.

C. Multiple-scattering analysis

In this section we present a quantitative analysis of the ARPEFS data based on multiple-scattering spherical wave calculations, after Barton, Robey, and Shirley.[14] The Taylor-series magnetic-quantum-number expansion approximation permits economical MSSW calculations and takes into account important physical aspects of the problem.

A MSSW calculation requires several input parameters, both structural parameters of adsorbate-substrate geometry and nonstructural parameters including atomic partial-wave phase shifts, Debye temperatures, mean free path, emission and polarization directions, detector aperture, experimental temperatures, and inner potential. The theory is most sensitive to the structural parameters, but the choice of the nonstructural parameters affects the accuracy of the derived structural information. We first consider the nonstructural parameters. The copper phase shifts were from previous calculations,[23,24] while the chlorine phase shifts were calculated from a modified program developed by Pendry[25] for LEED and a potential obtained from atomic Hartree-Fock wave functions, which were truncated at a muffin-tin radius $R_{\max}$. Values of $R_{\max}$ from 1.0 to 1.8 Å were used in the calculations and an optimum value of $R_{\max}$ was found to be 1.35 Å. Phase shifts at different values of $R_{\max}$ did not cause strong differences in the results of the MSSW analysis. The exchange potential was calculated in the $X\alpha$ approach with the factor α (0.723) used by Schwarz.[26] A total of 16 partial wave phase shifts for Cl was calculated from 40 to 600 eV.

The thermal effect was taken into account by a correlated Debye model which included surface-layer-dependent and anisotropic mean-square relative displacements (MSRD).[14] The copper bulk Debye temperature was taken at 343 K, while the copper surface Debye temperature was set to 243 K assuming that the surface copper atoms had an MSRD twice that of the bulk. The Debye temperature for the Cl overlayer was estimated to be 325 K from the Cu surface Debye temperature adjusted for the difference in masses. Actually, surface Debye temperatures for both Cl and Cu are varied in the calculations based on the above-estimated values. The mean free path was included in an exponential factor $e^{-r/\lambda}$, with $\lambda=ck$. The value of $c=0.753$ for Cu is similar to that for Ni.[27] In addition, the emission and polarization angles ($\pm 3°$), the experimental temperature (110 ± 10 K), and the inner potential (10 ± 5 eV) were allowed to vary in the calculations.

1. Site determination

Fourier analysis established a fourfold hollow adsorption site. Comparisons of the MSSW calculations with the experimental data confirm this result. The $\chi(k)$ curves for three unreconstructed adsorption geometries (atop, bridge, and fourfold hollow) were calculated using a Cl—Cu bond length of 2.41 Å derived from the Fourier analysis. The calculated curves are compared with the experimental data in Figs. 6 and 7 for the [001] and [011] directions, respectively. By visual inspection, the calculated curves from the fourfold hollow geometry most closely resemble the experimental data. Still, large differences exist even for the fourfold hollow geometry, based on these nonoptimized trial geometrical parameters. To derive a detailed quantitative structure, we therefore optimized both structural and nonstructural parameters to produce the best agreement between theoretical and experimental $\chi(k)$ curves.

2. Structural determination

First, both the [001] and [011] experimental $\chi(k)$ curves, at both temperatures, were smoothed by Fourier filtering out the high-frequency portion of the data (path-length differences larger than 16.5 Å). Although there were some real signals beyond 16.5 Å, the cutoff at this value retains all the major contributions from down to the fourth substrate layer and eliminates high-frequency noise at the same time, facilitating comparisons with the calculated curves. All subsequent comparisons of theory with experiment were done with filtered data, 2.0–16.5 Å for the [001] data, and 1.5–16.5 Å for the [001] data. The MSSW calculations were performed with the same path-length difference cutoffs.

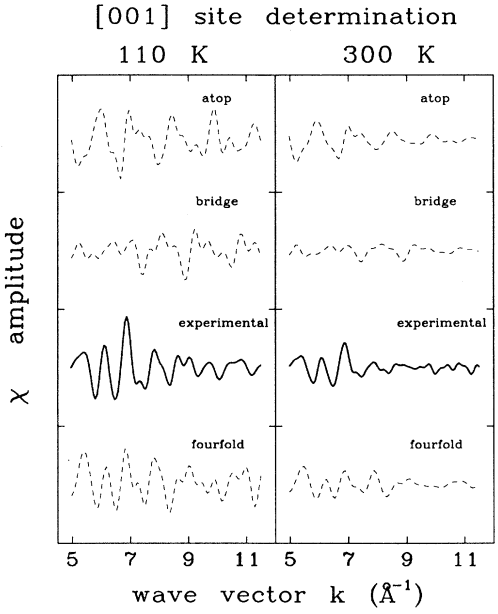

FIG. 6. Adsorption site determination for the [001] geometry at two temperatures. The experimental curves (solid lines) are compared to the MSSW calculated curves (dashed lines) for three unreconstructed adsorption geometries (atop, bridge, and fourfold hollow). The experimental data most closely resemble the fourfold hollow calculations at both temperatures.

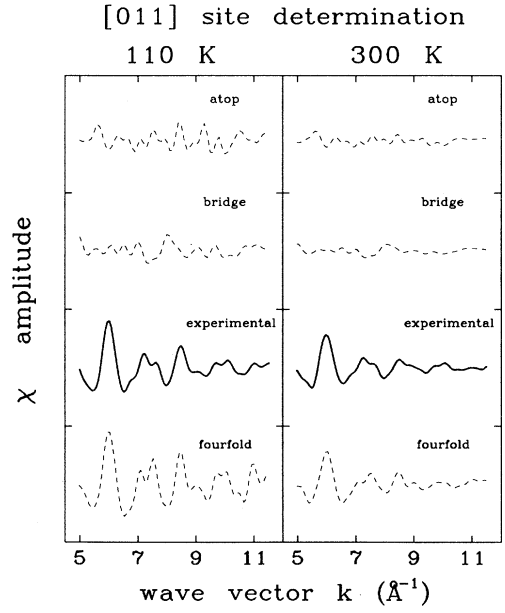

FIG. 7. Adsorption site determination for the [011] geometry at two temperatures. The notation is similar to Fig. 6. The experimental data most closely resemble the fourfold hollow calculations at both temperatures.

The comparison was based on an R-factor analysis, with optimum geometrical parameters being obtained when a minimum R factor, defined by

$$R=\frac{\int[\chi_E(k)-\chi_T(k)]^2dk}{\int\chi_T(k)^2dk}, \tag{6}$$

was reached. Here E and T denote experiment and theory. The R factors were calculated over the k range 5.0–11.0 Å^{-1}.

It would be ideal to search out a global minimum in a large parameter space by varying all the possible parameters simultaneously. Unfortunately, all the nonstructural and structural parameters together give too many variables to handle at one time. In early ARPEFS analyses, this problem was simplified by varying one or two structural parameters at a time, while most of nonstructural parameters were kept fixed. Because some parameters are coupled, finding a global minimum by this approach can be elusive. In the present study, an automatic routine was therefore used to search many more parameters simultaneously with a reasonable number of iterations. Normally, it took about 200–400 iterations to achieve a convergence of R factors for searching about five to nine parameters at a time. This routine started from an unreconstructed trial geometry with physically reasonable boundaries. The structural parameters obtained by varying different groups of parameters at a time with different initial guesses are very consistent, showing that a minimum found in this way should be an absolute minimum. Some of the nonstructural parameters were also varied along with the structural parameters, improving the accuracy of the structural parameters and allowing us to detect subtle changes in the surface structure.

No lateral substrate relaxation was included because of the $c(2\times2)$ structure of the Cl/Cu(001) system. We first optimized the following perpendicular distance parameters: the Cl-Cu(1) distance, the Cl-Cu(2a) distance to the atopped-site second layer copper, the Cl-Cu(2o) distance to the uncovered-site second layer copper, the Cl-Cu(3) distance, the "Debye temperatures" of Cl, in the parallel and perpendicular directions, respectively, the emission angle (polar angle) and the inner potential V_0. For convenience, we use a short notation [001]-(110 K) for the [001] data at 110 K, and similarly for other data sets. The Cl-Cu(4) distance was optimized from the [001]-(110 K) data. Nonstructural parameters such as the Debye temperatures, the emission angle, and the inner potential affected the extended fine structure more than did other nonstructural parameters, and they tended to be correlated with the structural parameters. Thus, all the major structural parameters and the important nonstructural parameters were taken as variables in the automatic routine. The emission angles were found to be $<1°$ off from 48° for the [011] data, and $<3°$ off the normal for the [001] data. The inner potential for the optimum geometry was 10±2 eV, and the experimental temperature was optimized to be 110±5 K. The structural parameters obtained from the four data sets were consistent, especially for the data at different temperatures

with a given geometry. R-factor minima lay in the small range $R=0.06-0.15$ in the various calculations.

The structural parameters determined from the above analysis are set out in Table I. The Cl-Cu(1) distance values lie within 0.01 Å among the four data sets, and the Cl-Cu(2*a*) distances are larger than the Cl-Cu(2*o*) distances within each data set. The R-factor minima were smaller for a given geometry at the lower temperature, due to the increased signal-to-noise ratio.

The directional sensitivity of ARPEFS and the sensitivity of a given data set to each structural parameter are displayed by two-dimensional error contour plots. Figure 8 shows contours for the [001]-(110 K) and [011]-(110 K) data, calculated by varying two parameters, Cl-Cu(1) and Cl-Cu(2*a*), while other parameters were fixed in their optimum values obtained previously. The [001] contour displays a very steep curvature when varying the Cl-Cu(2*a*) distance, indicating that the [001] data are more sensitive to Cl-Cu(2*a*), because there is a backscatterer Cu(2*a*) directly below Cl along the [001] direction. The [011] contour shows a greater sensitivity to the Cl-Cu(1) distance due to the existence of a backscatterer in the first copper layer directly behind Cl along the [011] direction. The contours generated by varying Cl-Cu(2*a*) and Cl-Cu(2*o*) for the [001]-(110 K) and [011]-(110 K) data are shown in Fig. 9. Not surprisingly, the [001] contour shows higher sensitivity to the Cl-Cu(2*a*) distance. However, a minimum along Cl-Cu(2*o*) is still well defined. The [011] contour exhibits a rather different shape. It shows similar sensitivities both to the Cl-Cu(2*a*) and the Cl-Cu(2*o*) distances with a relatively broad minimum, because the difference between the scattering angles for the uncovered-site and atopped-site copper atoms are not very significant, and the scattering amplitudes at these angles are relatively low.

As pointed out in the Fourier analysis, scattering off the third and the fourth copper layers makes significant contributions to the extended fine structure, especially for the [001]-(110 K) data. Figure 10 shows comparisons of the [001]-(110 K) data filtered out to 20 Å with the MSSW calculations at cutoffs in the path-length differences up to 10, 13, and 20 Å. By visual observation, the MSSW calculations for the 10- and 13-Å cutoffs, where the contributions from copper layers deeper than the third and fourth are excluded, respectively, do not adequately model the high-frequency portion of the experimental data, while the MSSW calculation up to 20-Å path-length difference compares more favorably. Here again, we demonstrate that the structural information from the deeper substrate layers is present in the extended fine structure and can be successfully modeled by the MSSW calculation including the scatterers from those layers.

Figure 11 shows a contour for the Cl-Cu(2*o*) and Cl-Cu(3) distances for the [001]-(110 K) data, which is more sensitive to the Cl-Cu(3) distance than to the Cl-Cu(2*o*) distance. The relatively steep curvature with respect to Cl-Cu(3) yields an accurate value for this parameter. Figure 12 presents a contour for Cl-Cu(3) vs Cl-Cu(4). The sensitivity to Cl-Cu(3) is expected to be larger than to Cl-Cu(4). Surprisingly, the sensitivity for the Cl-Cu(4) distance is still quite good. The [001]-(300 K) data set no large Fourier peaks at path-length differences greater than 10 Å (Fig. 4), and the Cl-Cu(3) distance derived from these data has a larger uncertainty. Thus, the lower temperature ARPEFS data improve the accuracy of the structural parameters for the deeper substrate layers.

3. *Error analysis*

The error contour plots described previously indicate the relative sensitivity of a given data set to a structural

TABLE I. Summary of the structural results (in Å) determined from MSSW analysis and comparisons with the LEED and SEXAFS results. The statistical errors associated with each parameter for the four data sets are given in parentheses (see Sec. III C 3). The structural parameter values in the upper panel are derived directly from fits of the data, while those in the lower panel were derived by subtracting two corresponding values above the line.

Parameter	$[001]_{110\ K}$	$[001]_{300\ K}$	$[011]_{110\ K}$	$[011]_{300\ K}$	Avg.[a] (stat)	Avg.[b] (scat)	This work[c] work	LEED	SEXAFS
Cl-Cu(1)	1.605(13)	1.612(14)	1.604(8)	1.601(9)	1.604(5)	1.606(4)	1.604(5)	1.60(3)	1.53(2)
Cl-Cu(2*a*)	3.451(8)	3.459(10)	3.441(25)	3.431(36)	3.453(6)	3.446(11)	3.453(11)		
Cl-Cu(2*o*)	3.413(19)	3.432(25)	3.390(30)	3.378(58)	3.412(13)	3.403(21)	3.412(21)		
Cl-Cu(3)	5.223(13)	5.237(23)	5.186(34)	5.178(81)	5.222(11)	5.206(25)	5.222(25)		
Cl-Cu(4)	7.023(22)				7.023(22)	7.023(22)	7.023(22)		
Cl-Cu					2.416(3)	2.418(3)	2.416(3)	2.41(2)	2.37(2)
Cu(1)-Cu2(*a*)					1.849(8)	1.840(12)	1.849(12)	1.85(3)	1.90(2)
Cu(1)-Cu(2*o*)					1.808(14)	1.797(21)	1.808(21)	1.85(3)	1.90(2)
Cu(2*a*)-Cu(3)					1.769(13)	1.760(27)	1.769(27)		
Cu(2*o*)-Cu(3)					1.810(17)	1.803(33)	1.810(33)		
Cu(3)-Cu(4)					1.801(25)	1.817(33)	1.801(33)		

[a]Statistical errors only: standard deviation.

[b]Standard deviation from the scatter of results.

[c]Final adopted values, with standard deviation taken as the higher of a and b above. Not included in these values and error estimate are any possible offset due to (unknown) systematic error.

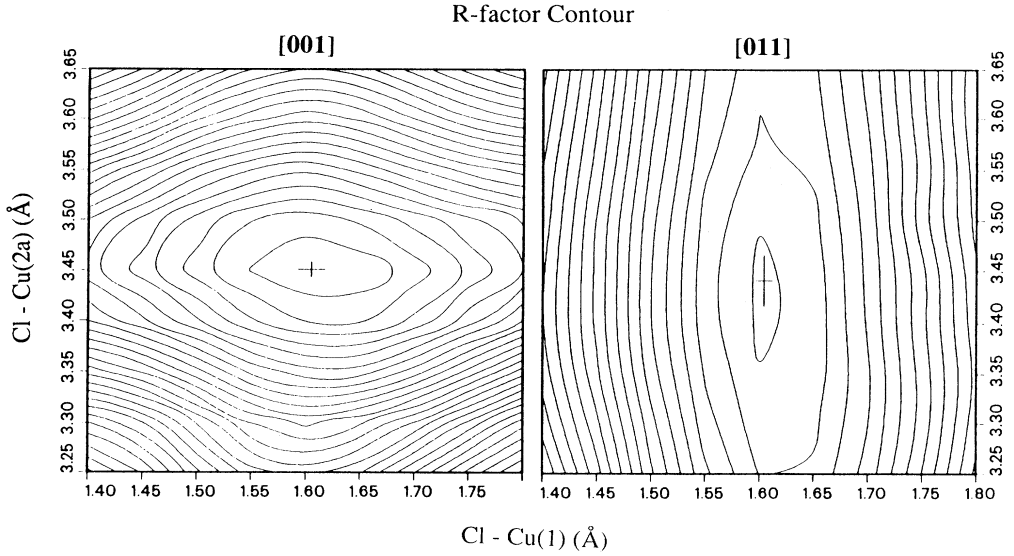

FIG. 8. *R*-factor contours of Cl-Cu(1) vs Cl-Cu(2*a*) for the [001] and [011] geometries at 110 K. For each contour, all the other parameters are kept at their optimum values. The minimum value of the *R* factor is 0.11 for the [001] geometry and 0.07 for the [011] geometry. The innermost contour line corresponds to an *R* factor of 0.20 for the [001] geometry and 0.10 for the [011] geometry. The contour interval is 0.10. The position of the *R*-factor minimum is marked by +, where the size of this mark represents the statistical error for each parameter (see Sec. III C 3).

parameter. However, it is important in structural determinations to evaluate the errors associated with each structural parameter. There are two kinds of error, statistical and systematic.

Statistical error analysis in nonlinear least-squares fitting is based mainly on the χ^2 method,[23,28] where χ^2 is defined by

$$\chi^2=\sum_j \left[\frac{1}{\sigma_j^2}[Y_j-Y(x_j)]^2\right] . \tag{7}$$

We shall follow the universal convention and retain the symbol χ here, not to be confused with $\chi(k)$ or $\chi(E)$. Here σ_j is the standard deviation of each data point Y_j, $Y(x_j)$ is the fitting function. A reduced χ^2 is given by

$$\chi_v^2=\frac{\chi^2}{v} , \tag{8}$$

with $v=N-n-1$ representing the number of degrees of freedom, N the number of data points, and n the number of fitting parameters. The optimum values of parameters

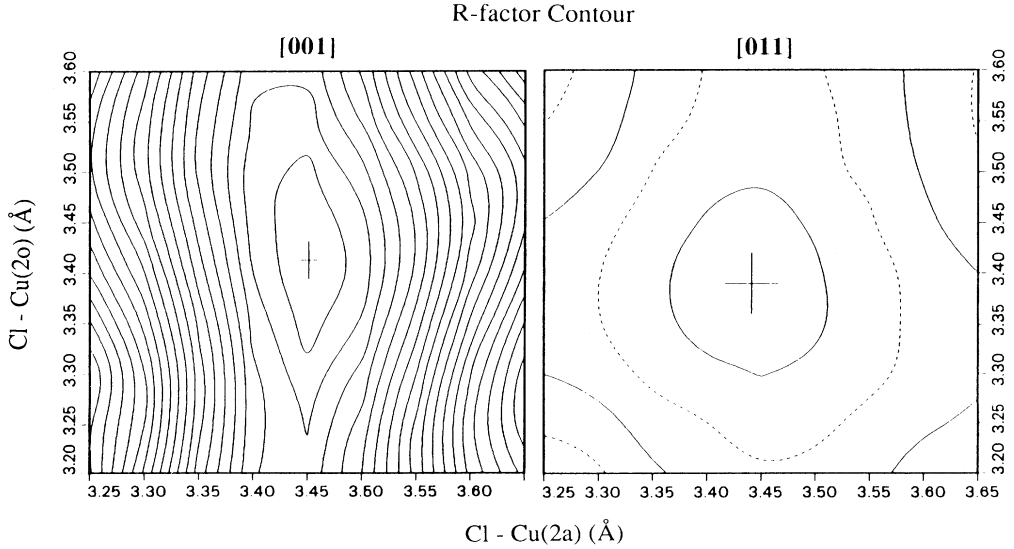

FIG. 9. *R*-factor contours of Cl-Cu(2*a*) vs Cl-Cu(2*o*) for the [001] and [011] geometries at 110 K, as in Fig. 8. The minimum value of the *R* factor is 0.11 for the [001] geometry and 0.07 for the [011] geometry. The contour interval between solid curves is 0.10.

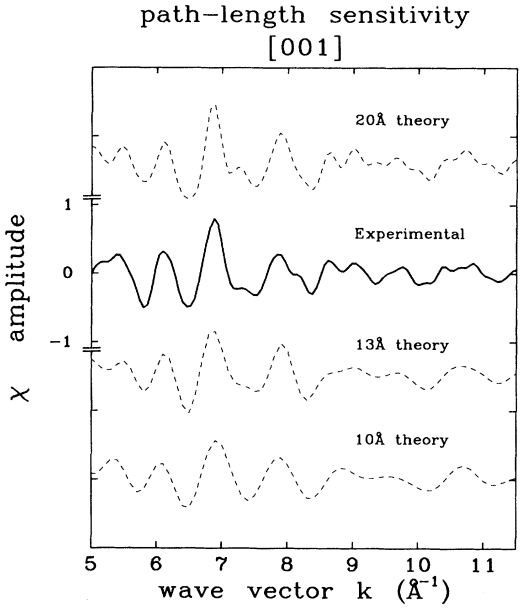

FIG. 10. Illustration of ARPEFS path-length sensitivity beyond 10 Å. The 20-Å calculated curve models the high-frequency structure of the data very well, while the 10- and 13-Å curves do not.

are obtained by minimizing χ^2 with respect to each parameter P_j simultaneously. If the variation of χ^2 with respect to each parameter is independent of the values of the others, and the reduced $\chi^2_v \approx 1$, then the statistical error associated with each parameter can be obtained from the curvature of the χ^2 parabola: that is, the standard deviation, σ_{P_j}, of a parameter P_j can be expressed as

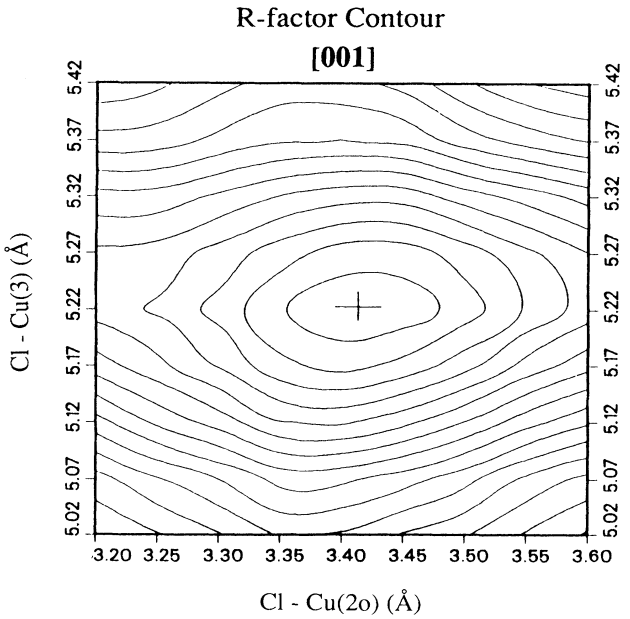

FIG. 11. R-factor contours of Cl-Cu(2o) vs Cl-Cu(3) for the [001] geometry at 110 K. The minimum value of the R factor is 0.11 with a contour interval of 0.05, and the innermost contour line corresponds to $R=0.15$.

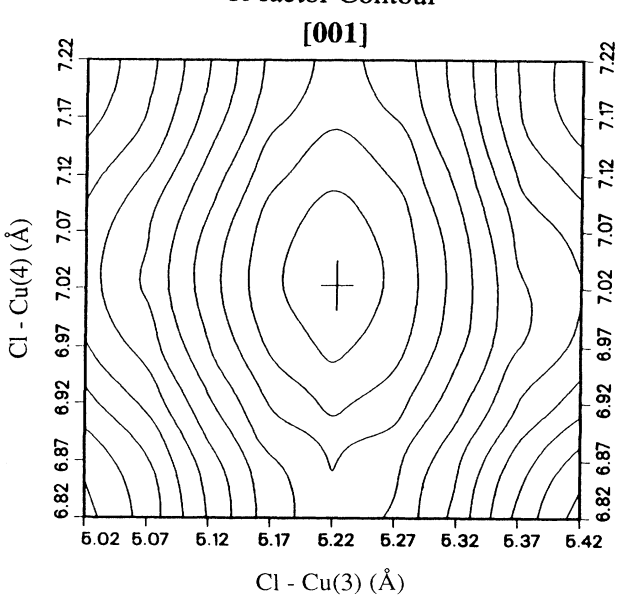

FIG. 12. R-factor contur of Cl-Cu(3) vs Cl-Cu(4) for the [001] geometry at 110 K, similar to Fig. 11.

$$\sigma^2_{P_j} = \frac{2}{\partial^2\chi^2/\partial P_j^2} \ . \tag{9}$$

If χ^2 is a parabolic function, $\chi^2 = aP^2 + b$, then

$$\sigma^2_{P_j} = \frac{1}{a} \ . \tag{10}$$

The procedure for extracting structural parameters by using the automatic search routine can be considered as the nonlinear least-squares fitting of theoretical $\chi(k)$ functions to experimental data while optimizing several parameters simultaneously. No correlations between the structural parameters were found from the shapes of the error contour plots. Therefore, in principle, errors could be estimated by the χ^2 method. However, even for the best ARPEFS fit, the difference between theory and experiment exceeds statistical expectations, and $\chi^2_{v_{\min}} > 1$, where $\chi^2_{v_{\min}}$ is the value at the minimum of the χ^2 parabola. In this case, the standard deviation of a parameter can be modified by multiplying $\sigma^2_{P_j}$ with $\chi^2_{v_{\min}}$ $(=b/v)$ to get

$$\sigma'^2_{P_j} = \frac{b}{av} \ . \tag{11}$$

Thus, the statistical errors are determined by the χ^2 curvature a (the sensitivity to parameters), its minimum value b (the quality of fits), and the number of degrees of freedom v. Steeper curvature, smaller minima of the χ^2 parabola, and more degrees of freedom give smaller statistical errors.

The parameters a and b in Eq. (11) have straightforward meanings, but v cannot be evaluated so simply. The relation $v = N - n - 1$ is valid only if the N data points are independent. In a typical ARPEFS $\chi(k)$ curve there may

be 100 or more data points, but the curve could be described by a substantially smaller number of points. The exact number needed, $N_{\min}$, and therefore the values of $v = N_{\min} - n - 1$ and σ, can be estimated in several ways, which yield slightly different results. In this work we use a method based on a "spline-interpolation" step in the data analysis. This step is the interpolation of the raw $\chi(k)$ data onto an evenly spaced mesh in k prior to Fourier transformation and simulation. $N_{\min}$ is determined by reducing the mesh interval until the interpolated curve matches the raw data "curve" within the standard deviation σ_j of each data point. Application of this method to the present 110-K curves yielded $N_{\min}([001]) \sim 48$ and $N_{\min}([011]) \sim 40$. This difference was expected because for [001] the $\chi(k)$ curve shows more structure.

In summary, the *statistical* error σ_{P_j} in a given parameter P_j depends upon v, varying as $v^{-1/2}$ [Eq. (11)]. We note that other methods of estimating v might give somewhat different results. However, even a factor-of-2 difference in v would only change the statistical error estimate by $\sqrt{2}$. We therefore believe that this analysis gives a satisfactory estimate of the statistical error.

Table I lists, in columns 2–5 (upper panel), the statistical errors (standard deviations) of each parameter for the four data sets, determined as described above. Column 6 gives the average value of each parameter determined by suitable weighting of the values in columns 2–5, using standard statistical methods.

Scatter in the values of each derived parameter, among the four data sets, can also be used to estimate the standard deviation in the mean value. In fact, if we did not already have a good estimate of our statistical σ_{P_j}, this would be our *only* way to assess them. While four values cannot simulate a Poisson, let alone a Gaussian, distribution, use of the "scatter" equation,

$$\sigma_j^2 = \tfrac{1}{4} \sum_i (P_{ji} - \bar{P}_j)^2 \tag{12}$$

gives an indication of the error to be associated with scatter in the derived values, *per se*. Column 7 in Table I lists the simple averages of the derived parameters, taken from columns 2–5, together with standard deviations determined from Eq. (12).

The close agreement between the derived values of parameters in columns 6 and 7, in which the statistical errors were estimated in very different ways together with the small standard deviations, reinforces our belief that the *statistical* uncertainty in these parameters is quite small. Column 8 lists our best values for these parameters, which we take as the *values* in column 6—clearly preferred because the individual value from which they are derived are weighted—and the errors from the larger of those in columns 6 and 7. It seems inescapable that *systematic* errors contribute to the scatter of the derived parameter values, and we believe that this effect shows up in the generally larger errors in column 8. Conversely these errors probably give a reasonable estimate of the uncertainties due to combined statistical and systematic errors, with one exception, discussed below. We can estimate the uncertainty due to these systematic errors, which might include the effect of misalignment, background evaluation errors, etc., from the differences between the mean values in columns 6 and 7. By this criterion, these systematic errors are also quite small.

The above discussion of systematic errors should apply to errors which lead to *random* scatter in the results. If there are also other systematic errors present which bias the derived parameter values either high or low, such errors will of course not show up even in column 7.

We cannot identify any systematic errors in the *measurements* that would bias the derived interatomic distances high or low. Path-length differences are most closely related to the electron's momentum vector k, which follows from the kinetic energy. There are always experimental errors, but no bias, associated with these parameters.

The theoretical modeling process could in principle introduce bias, by systematically overestimating or underestimating a nonstructural parameter such as the crystal potential V_0 or the scattering phase shift ϕ_j. We note that, in contrast to EXAFS, for which a shift ΔR arises from the source-atom phase shift (and is evaluated using model compounds), there is no source-atom phase shift in the ARPEFS scattering process because of cancellation: the direct and scattered waves both leave the source atom only once. As for V_0 and ϕ_j, we know of no reason to expect a large bias in R values from these parameters.

Finally, the theoretical modeling process could introduce bias by omitting a physical process. Our candidate here would be dynamic screening changes as the source atom decays by an Auger cascade while the photoelectron is still close. The integrated effect might vary monotonically with k, introducing some bias. Consideration of such processes might be a fruitful topic for theoretical study, but to attribute a systematic error based on present knowledge would be too speculative.

In summary, we find no evidence for error sources that would systematically bias our results, and we therefore quote as our best values and standard deviations the values given in column 8 of Table I. In comparing these results, especially the errors, with values derived from other studies, caution should be exercised, because the quoted errors are often not standard deviations. In electing to quote standard deviations, which vary in our results from 0.003 to 0.033 Å, we have sought to retain this variation, and have eschewed the temptation to quote all errors as $\sim \pm 0.02$ Å, in hopes of advancing a more quantitative approach to estimating errors.

4. Results

The best fits to the experimental $\chi(k)$ curves are shown in Figs. 13 and 14 for the [001] and [011] data, respectively. Agreements between the theoretical and experimental curves are excellent. Figure 15 shows the top and side views of the $c(2\times2)$Cl/Cu(001) structure, labeling the layer spacing for which fitted values are listed in Table I. The Cl-Cu(1) distance of 1.604(5) Å, fits with a Cl—Cu bond length of 2.416(3) Å. The Cl-Cu(2*a*) distance of 3.453(11) Å then gives a Cu(1)-Cu(2*a*) distance of

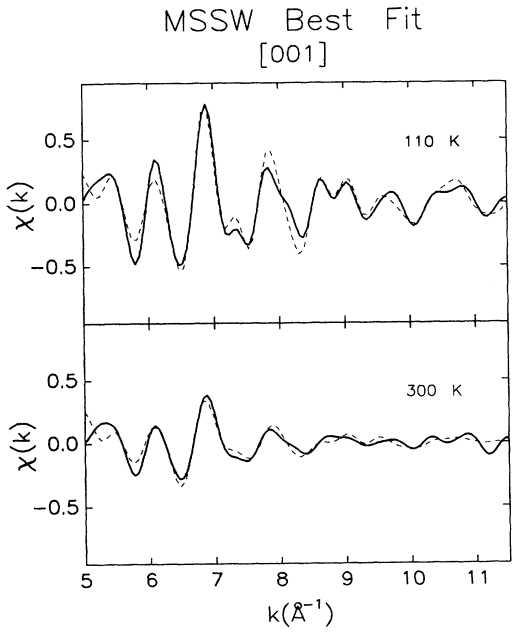

FIG. 13. The best fits of the MSSW calculations (dashed curves) to the fitted (16.5-Å) ARPEFS data (solid curves) for the [001] geometry at two temperatures, 110 and 300 K.

1.849(12) Å, showing an expansion from the bulk value (1.807 Å), while the Cl-Cu(2*o*) distance of 3.412(21) Å yields a Cu(1)-Cu(2*o*) distance of 1.808(21) Å. The difference between Cl-Cu(2*a*) and Cl-Cu(2*o*) of 0.041(24) Å reveals a small corrugation of the second copper layer. Furthermore, the Cl-Cu(3) and Cl-Cu(4) distances were

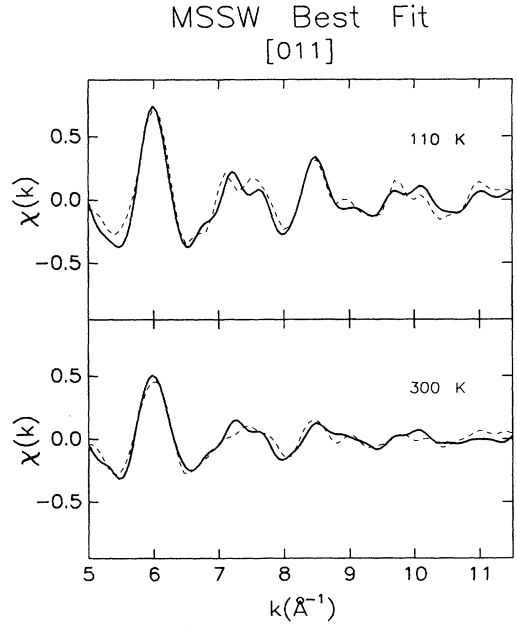

FIG. 14. The best fits of the MSSW calculations (dashed curves) to the filtered (16.5-Å) ARPEFS data (solid curves) for the [011] geometry at two temperatures, 110 and 300 K.

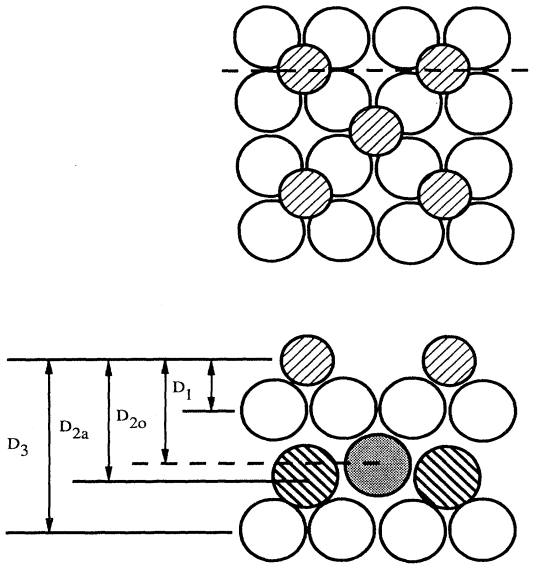

FIG. 15. Top and side views of the c(2×2)Cl/Cu(001) structure. The side view (lower panel) corresponds to a cut in the plane shown by the dashed line in the top view (upper panel), while D_1, D_{2o}, D_{2a}, and D_3 represent the perpendicular distances of Cl-Cu(1), Cl-Cu(2*o*), Cl-Cu(2*a*), and Cl-Cu(3), respectively, as described in the text.

found to be 5.222(25) and 7.023(22) Å, respectively, giving the Cu(3)-Cu(4) distance of 1.801(33) Å and Cu(2*o*)-Cu(3) distance of 1.810(33) Å, in good agreement with the bulk spacing. By difference, the Cu(2*a*)-Cu(3) distance of 1.769(27) Å shows a contraction from the bulk value. The magnitude of this contraction in Cu(2*a*)-Cu(3) is approximately equal to that of the expansion in Cu(1)-Cu(2*a*). Assuming the fourth copper layer is in the bulk position, from the bulk-like spacings of Cu(3)-Cu(4) and Cu(2*o*)-Cu(3), we infer that the third-layer and uncovered-site second-layer copper atoms must also lie in the bulk positions.

IV. DISCUSSION

The Cl-Cu(1) distance of 1.604(5) Å obtained from the ARPEFS study is in excellent agreement with the LEED result,[1] but not with the SEXAFS result of 1.53 Å.[2,17] We have calculated $\chi(k)$ curves based on this SEXAFS value for the Cl-Cu(1) distance and the other parameters as obtained from the current ARPEFS study. These curves are compared with two experimental $\chi(k)$ curves in Fig. 16, to test the sensitivity of ARPEFS to the Cl-Cu(1) parameter. By visual inspection, the agreement is very poor, the *R* factors are about 3 and 5 times larger than those for the [001] and the [011] ARPEFS optimum geometries, respectively. There are large shifts between the theoretical and experimental curves for the [011] geometry, but not so much for the [001] geometry, because scattering from the Cu(2*a*) dominates the [001] $\chi(k)$ curve. In these fits, the inner potential V_0 was optimized to be $\sim$10 eV from previous studies.[5,27] Even if a larger value of 15 eV was used in an effort to reduce the

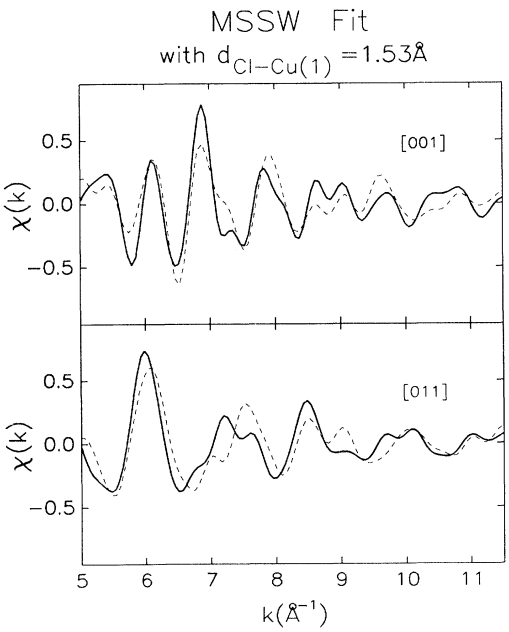

FIG. 16. Comparisons of the filtered (16.5-Å) ARPEFS data (solid curves) to the MSSW calculations (dashed curves) for the [001] and [011] geometries at 110 K. The MSSW curves are calculated with A Cl-Cu(1) distance of 1.53 Å as obtained from a previous SEXAFS study, while all the other parameters are kept fixed at their optimum values.

shifts for the [011] geometry, the agreement is still poor. It is also of interest to compare the Cl—Cu bond length as obtained from SEXAFS and ARPEFS, because this is the parameter which SEXAFS measures most directly. From Table I we note that the SEXAFS value of 2.37(2) Å is only 1.9% below what we believe to be the correct value of 2.416(3) Å: quite close by even fairly recent standards of surface structure determinations.

Since the third copper layer remains in the bulk position, by subtracting the bulk interlayer spacing twice from the Cl-Cu(3) distance of 5.222(25) Å, we can determine the distance of Cl above the bulk-extrapolated first copper layer to be 1.608(25) Å, in excellent agreement with our Cl-Cu(1) distance of 1.604(5) Å with the surface reconstruction taken into account, and the result 1.60(4) Å obtained from the x-ray standing wave measurement.[17] Therefore, we conclude that there is no outward relaxation of the first copper layer, contrary to the results of Patel *et al.*[17] However, it has been shown that there was indeed an expansion of the topmost interlayer substrate spacing from three different techniques: ARPEFS, LEED, and SEXAFS. This expansion is mainly due to the downward relaxation of the second copper layer, based on the facts that there was no relaxation of the first copper layer and there was a contraction in the Cu(2a)-Cu(3) distance. This demonstrates that the lower-temperature ARPEFS study can prove relaxation of not only the first substrate layer but also deeper layers relative to the bulk positions. As yet, there is no theory available to predict adsorbate-induced relaxations. Perhaps the results obtained from this work can provide some experimental guidance.

Studies on the clean Cu(001) surface[29,30] showed a (1.1±0.4)% *contraction* of the topmost interlayer spacing, while both LEED (Ref. 1) and this work showed an expansion of about 2% when Cl adsorbs on the clean surface, as compared with the bulk spacing, giving an expansion of about 3% with respect to the spacing of the clean Cu(001) surface. The (1.1±0.4)% contraction of the clean surface resulted mostly from the inward movement of the first copper layer relative to the bulk position, according to a theoretical study.[31] Thus, with adsorption of Cl on the clean surface, the outward movement of the first copper layer and the downward movement of the second copper layer lead to a 3% expansion between the first and the second copper layers. Furthermore, the ARPEFS study revealed a small corrugation of the second copper layer, not observed by other techniques. This corrugation is understandable because atoms in the even substrate layers are in two symmetry-inequivalent atomic sites relative to the adatoms for the $c(2\times2)$ structure.

The occurrence of the corrugation and expansion induced by the adsorption of Cl indicates that chemical bonding between the adsorbate and the substrate atoms modifies the surface and near-surface structure, inducing relaxation of the substrate layers. The mechanism of the relaxation may be very complicated, but we propose a simple physical picture. The metal-metal bond weakening induced by adsorption is probably the main factor in causing the expansion of the topmost interlayer spacing. In the case of $c(2\times2)$Cl/Cu(001), the expansion due to metal-metal bond weakening is expected to affect the atopped-site atoms directly below Cl more than the uncovered-site atoms, causing corrugation of the second copper layer, where the atopped-site atoms are displaced further away from the adsorbate. This kind of corrugation has been observed in other systems studied by ARPEFS.[27,32] In addition, a recent LEED study on $c(2\times2)$O/Ni(001) (Ref. 33) showed a similar corrugation and an even larger expansion of the second substrate layer. In the O/Ni(001) system, the adsorbate O sits much closer to the metal substrate surface than the Cl atom, yielding a stronger interaction between the adsorbate and the metal substrate surface. A more complete understanding of the substrate surface relaxation induced by adsorbates would require a better knowledge of the nature of the surface chemical bonding.

V. CONCLUSION

We have presented a detailed study of the $c(2\times2)$Cl/Cu(001) adsorption geometry and substrate surface relaxation using low-temperature ARPEFS. Fourier analysis and the multiple-scattering spherical-wave analysis were applied in this study. Fourier analysis yielded the adsorption site and the qualitative structural information, based on interpreting the features in the Fourier spectra with a single-scattering model. Multiple-scattering analysis yielded more quantitative structural information by comparing the experimental data with the MSSW calculations based on the R-factor

analysis. We conclude that the Cl atom adsorbs in the fourfold hollow site 1.604(5) Å above the first copper layer, giving a Cl—Cu bond length of 2.416(3) Å, in excellent agreement with the LEED result.[1] We have also observed that there is a 2% expansion of the separation between the first copper layer and the second atopped-site copper layer, and a small corrugation of the second copper layer where the atopped-site copper atoms are further away from the adsorbate Cl atom.

Real features in the Fourier spectra of the lower-temperature data can be seen at path-length differences greater than 15 Å. The experimental data can be successfully modeled by the MSSW calculations by considering the path-length differences up to 16.5 Å. The lower-temperature ARPEFS study has provided accurate near-surface structural parameters for the deeper substrate layers, 5.222(25) Å for the distance of Cl to the third copper layer, 7.023(22) Å for the distance of Cl to the fourth copper layer, yielding a bulklike interlayer spacing between the third and the fourth copper layers. More significantly, no relaxation of the $c(2\times2)$Cl-covered first copper layer with respect to the bulk position has been observed from the accurate near-surface structural information in the current work, which is inconsistent with the previous result obtained with a combination of the x-ray standing wave and SEXAFS techniques.[17] Instead, the downward relaxation of the second atopped-site copper layer results in an expansion of the topmost interlayer spacing, while the second uncovered-site copper layer remains in the bulk position.

We have demonstrated that low-temperature ARPEFS can probe deeper substrate layers, where information about the substrate surface relaxations relative to the bulk positions can be obtained. Therefore, low-temperature ARPEFS holds the promise to completely and accurately map out surface and near-surface structures for adsorbate systems.

ACKNOWLEDGMENTS

L.Q.W. wishes to thank Dr. M. A. Van Hove and Dr. Z. Hussain for valuable discussions. D.A.S. thanks the Alexander von Humboldt Foundation for partial support and Professor G. Kaindl and Professor E. Mattias for their hospitality during his stay in Fachbereich Physik, Freie Universität Berlin. This work was supported by the Director, Office of Energy Research, Office of Basic Energy Sciences, Chemical Sciences Division of the U.S. Department of Energy under Contract No. DE-AC03-76SF00098. The experiments were performed at the Stanford Synchrotron Radiation Laboratory, which is supported by the U.S. Department of Energy's Office of Basic Energy Sciences.

*Present address: Department of Physics, Zhejiang University, Hangzhou, Zhejiang, China.

[1]F. Jona, D. Westphal, A. Goldmann, and P. M. Marcus, J. Phys. C **16**, 3001 (1983).
[2]P. H. Citrin, D. R. Hamann, L. F. Mattheiss, and J. E. Rowe, Phys. Rev. Lett. **49**, 1712 (1982).
[3]J. F. van der Veen, Surf. Sci. Rep. **5**, 199 (1985).
[4]D. P. Woodruff, D. L. Seymour, C. F. McConville, C. E. Riley, M. D. Crapper, and N. P. Prince, Phys. Rev. Lett. **58**, 1460 (1987).
[5]J. J. Barton, C. C. Bahr, S. W. Robey, Z. Hussain, E. Umbach, and D. A. Shirley, Phys. Rev. B **34**, 3807 (1986).
[6]J. J. Barton, C. C. Bahr, Z. Hussain, S. W. Robey, J. G. Tobin, L. E. Klebanoff, and D. A. Shirley, Phys. Rev. Lett. **51**, 272 (1983).
[7]A. Liebsch, Phys. Rev. Lett. **32**, 1203 (1974).
[8]A. Liebsch, Phys. Rev. B **13**, 544 (1976).
[9]S. Kono, C. S. Fadley, N. F. T. Hall, and Z. Hussain, Phys. Rev. Lett. **41**, 117 (1978).
[10]D. P. Woodruff, D. Norman, B. W. Holland, N. V. Smith, H. H. Farrell, and M. M. Traum, Phys. Rev. Lett. **41**, 1130 (1978).
[11]S. D. Kevan, D. H. Rosenblatt, D. R. Denley, B.-C. Lu, and D. A. Shirley, Phys. Rev. Lett. **41**, 1505 (1978).
[12]S. D. Kevan, D. H. Rosenblatt, D. R. Denley, B.-C. Lu, and D. A. Shirley, Phys. Rev. B **20**, 4133 (1979).
[13]D. H. Rosenblatt, J. G. Tobin, M. G. Mason, R. F. Davis, S. D. Kevan, D. A. Shirley, C. H. Li, and S. Y. Tong, Phys. Rev. B **23**, 3828 (1981).
[14]J. J. Barton, S. W. Robey, and D. A. Shirley, Phys. Rev. B **34**, 778 (1986).
[15]L. J. Terminello, X. S. Zhang, Z. Q. Huang, S. Kim, A. E. Schach von Wittenau, K. T. Leung, and D. A. Shirley, Phys. Rev. B **38**, 3879 (1988).
[16]F. Sette, C. T. Chen, J. E. Rowe, and P. H. Citrin, Phys. Rev. Lett. **59**, 311 (1987).
[17]J. R. Patel, D. W. Berreman, F. Sette, P. H. Citrin, and J. E. Rowe, Phys. Rev. B **40**, 1330 (1989).
[18]Z. Hussain, E. Umbach, D. A. Shirley, J. Stohr, and J. Feldhaus, Nucl. Instrum. Methods **195**, 115 (1982).
[19]S. D. Kevan, Ph.D. thesis, University of California, Berkeley, 1980; and (unpublished).
[20]X. S. Zhang, L. J. Terminello, S. Kim, Z. Q. Huang, A. E. Schach von Wittenau, and D. A. Shirley, J. Chem. Phys. **89**, 6538 (1988).
[21]M. O. Krause and J. H. Oliver, J. Phys. Chem. Ref. Data **8**, 329 (1979).
[22]P. A. Lee, P. H. Citrin, P. Eisenberger, and B. M. Kincaid, Rev. Mod. Phys. **53**, 769 (1981).
[23]C. C. Bahr, J. J. Barton, Z. Hussain, S. W. Robey, J. G. Tobin, and D. A. Shirley, Phys. Rev. B **35**, 3773 (1987).
[24]P. J. Orders and C. S. Fadley, Phys. Rev. B **27**, 781 (1983).
[25]J. B. Pendry, *Low Energy Electron Diffraction* (Academic, London, 1974).
[26]K. Schwarz, Phys. Rev. B **5**, 2466 (1972).
[27]S. W. Robey, J. J. Barton, C. C. Bahr, G. Liu, and D. A. Shirley, Phys. Rev. B **35**, 1108 (1987).
[28]P. R. Bevington, *Data Reduction and Error Analysis for the Physical Sciences* (McGraw-Hill, New York, 1969), Chap. 11.
[29]H. L. Davis and J. R. Noonan, J. Vac. Sci. Technol. **20**, 842 (1981).
[30]J. R. Noonan and H. L. Davis, Bull. Am. Phys. Soc. **27**, 237 (1982).
[31]J. F. van der Veen and M. A. Van Hove, *Structure of Surfaces 2* (Springer, Heidelberg, 1988).
[32]A. E. Schach von Wittenau, L. Q. Wang, Z. G. Ji, Z. Q. Huang, T. Shulman, and D. A. Shirley (unpublished).
[33]W. Oed, H. Lindner, U. Starke, K. Heinz, K. Muller, and J. B. Pendry, Surf. Sci. **224**, 179 (1989).